NANO LETTERS

xxxx
Vol. 0, No. 0
A−F

Fast, Completely Reversible Li Insertion in Vanadium Pentoxide Nanoribbons

Candace K. Chan,[†] Hailin Peng,[‡] Ray D. Twesten,[§] Konrad Jarausch,[||] Xiao Feng Zhang,[||] and Yi Cui*,[‡]

Department of Chemistry and Department of Materials Science and Engineering, Stanford University, Stanford, California 94305, Gatan, Inc., 5933 Coronado Lane, Pleasanton, California 94588, and Electron Microscope Division, Hitachi High Technologies America, Inc., 5100 Franklin Drive, Pleasanton, California 94588

Received December 8, 2006

ABSTRACT

Layered-structure nanoribbons with efficient electron transport and short lithium ion insertion lengths are promising candidates for Li battery applications. Here we studied at the single nanostructure level the chemical, structural, and electrical transformations of V_2O_5 nanoribbons. We found that transformation of V_2O_5 into the ω-$Li_3V_2O_5$ phase depends not only on the width but also the thickness of the nanoribbons. Transformation can take place within 10 s in thin nanoribbons, suggesting a Li diffusion constant 3 orders of magnitude faster than in bulk materials, resulting in a significant increase in battery power density (360 C power rate). For the first time, complete delithiation of ω-$Li_3V_2O_5$ back to the single-crystalline, pristine V_2O_5 nanoribbon was observed, indicating a 30% higher energy density. These new observations are attributed to the ability of facile strain relaxation and phase transformation at the nanoscale. In addition, efficient electronic transport can be maintained to charge a $Li_3V_2O_5$ nanoribbon within less than 5 s. These exciting nanosize effects can be exploited to fabricate high-performance Li batteries for applications in electric and hybrid electric vehicles.

The increasing demand for rechargeable batteries for portable electronic devices and the need for high energy and power density batteries for electric vehicles and hybrid electric vehicles have generated significant research interest in lithium batteries. In addition to searching for compositionally new electrode materials,[1,2] the approach of structuring material in the nanoscale has also gained attention for improved lithium batteries. Because of the large interfacial contact area with the electrolyte, nanostructured electrodes shorten Li-ion insertion distances, leading to enhanced power density compared to bulk battery counterparts.[3] Battery devices fabricated out of ensembles of nanostructured V_2O_5,[4−6] Fe_3O_4,[7] Co_3O_4,[8] and TiO_2(B)[9] have shown higher power rates. Li storage mechanisms not possible with bulk materials can occur as the size scale decreases. For example, the pure capacitance effect due to large surface area can increase energy capacities by 100%;[10] a conversion instead of intercalation mechanism can take place in nanocrystalline oxides and provide higher energy anodes.[11]

We study one-dimensional nanowire (NW) structures[12−14] because they can efficiently transport charge carriers while maintaining a large surface-to-volume ratio that enhances contact with electrolyte. We chose vanadium pentoxide (V_2O_5) as a model system for single nanostructure measurements because V_2O_5 has been a promising battery cathode material and widely studied. The orthorhombic crystal structure of V_2O_5 can be described as layers of VO_5 square pyramids that share edges and corners[15] (Figure 1A, top). The sixth V−O bond in the *c*-direction consists of weak electrostatic interactions, which facilitate the insertion of various ions and molecules between the layers.[16] Li-ion insertion and electronic transport occur more easily along the *a*−*b* plane rather than through the layers of the *c*-axis.[17] Previous ensemble NW studies have thus focused on maximizing the electrolyte contact area and decreasing the Li-ion diffusion distance in the *a*−*b* planes, although the effect of the *c*-dimension has been overlooked.

V_2O_5 NWs were synthesized by a chemical vapor transport method (Supporting Information). In a typical synthesis, V_2O_5 powder was placed in the center of a tube furnace with temperature set at 900 °C; 150 sccm O_2 carrier gas transported the V_2O_5 vapor downstream to Si-collecting substrates at a temperature range of 450−500 °C (Figure S1 in Supporting Information). Scanning electron microscopy (SEM) images on as-grown samples showed a high yield of NWs covering the whole substrate surface (Figure 1B). High-resolution SEM indicated that these NWs have a nanoribbon

* To whom correspondence should be addressed. E-mail: yicui@stanford.edu.
[†] Department of Chemistry, Stanford University.
[‡] Department of Materials Science and Engineering, Stanford University.
[§] Gatan, Inc.
[||] Hitachi High Technologies America, Inc.

10.1021/nl062883j CCC: $37.00
Published on Web 01/26/2007

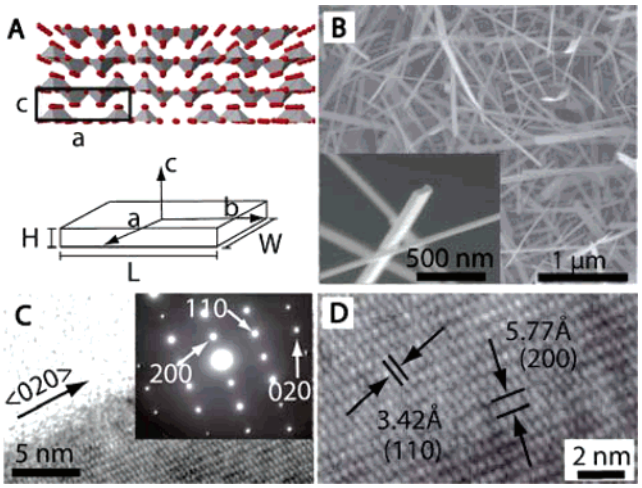

Figure 1. (A) Top: Layered crystal structure of bulk V_2O_5 with boxed region indicating the unit cell. The red circles represent O atoms and the gray pyramids illustrate the VO_5 units (V atoms not shown). Bottom: Schematic of how the axes are oriented with respect to a V_2O_5 NR. (B) SEM image of V_2O_5 NRs growing off of a silicon nitride substrate. High-resolution SEM (inset) reveals a rectangular cross-section, indicating a ribbon shape. (C−D) High-resolution TEM images of V_2O_5 NR (C) Inset shows SAED of NR looking down the ⟨001⟩ zone axis. The (020) spot is parallel to the length of the NR, indicating the growth direction. (D) Lattice fringes are 3.42 Å and 5.77 Å, corresponding to the (110) and (200) planes, respectively.

(NR) morphology (Figure 1B, inset). These NRs were found to be 20−150 nm in height (H) from atomic force microscopy (AFM) measurements (Figure S2), 50 nm to several μm in width (W), and with lengths (L) up to 500 μm. The crystal structure of the NRs was identified using X-ray diffraction (XRD) and transmission electron microscopy (TEM). The XRD pattern (Figure S3) showed that the NRs were crystalline and matched the orthorhombic form of V_2O_5. High-resolution TEM characterization (Figure 1C and D) and selected area electron diffraction (SAED) (Figure 1C, inset) revealed that the NRs were single-crystalline, with the length along the *b*-axis, width along the *a*-axis, and the *c*-axis corresponding to the layers making the height of the NRs (Figure 1A, bottom). Because of this structure, V_2O_5 NRs tend to lay down with the *c*-axis parallel to the electron beam when they are transferred onto the TEM substrate. We did not use catalysts in the synthesis, and the formation of these NRs is likely through a vapor−solid process. The formation mechanism of the NR shape is attributed to the anisotropic bonding of the V_2O_5 layered structure. In V_2O_5, the ⟨010⟩ is the fastest growth direction and ⟨001⟩ the slowest due to the weak *c*-axis bonding. Indeed, the 1D nanoribbon structure has been observed in sol−gel and hydrothermal methods,[18] aerogels and xerogels,[10,19] and electrospinning techniques.[20]

To insert Li-ions into V_2O_5 NRs for further compositional, structural, and electronic transformation studies, we used a chemical lithiation method (Supporting Information). The Li insertion was done by immersing the NRs into an *n*-butyllithium (BuLi) reagent for the desired amount of time in inert atmosphere followed by extensive washing. This chemical lithiation method can give nearly the same results as electrochemical lithiation and determine the full lithiation

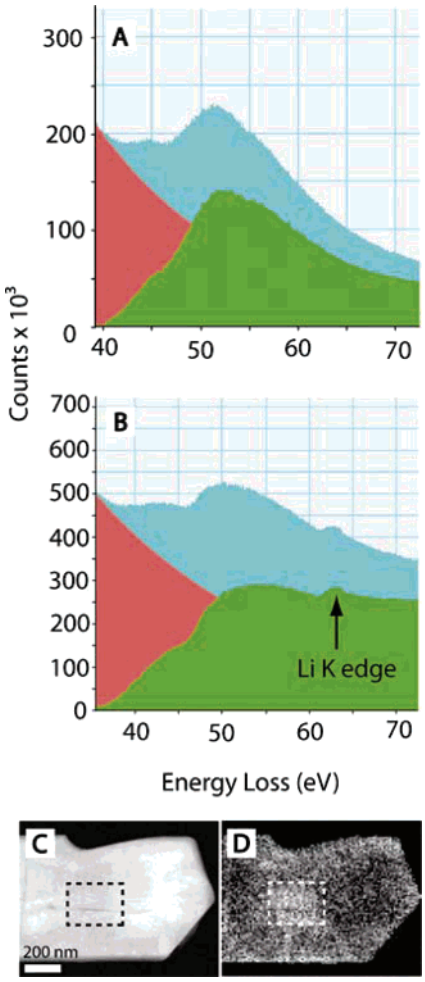

Figure 2. (A−B) EELS spectra of NRs with background extrapolated using log polynomial law fitting. The pink is the background, the blue is the total signal, and the green is extracted NR signal. (A) Spectrum taken from pristine V_2O_5 NR with V M45-edge onset seen at ∼37 eV. (B) Spectrum taken from $Li_xV_2O_5$ NR with the V M45-edge onset seen at ∼37 eV and Li K resonance at ∼62 eV. The Li K resonance is not observed in the pristine NR spectrum. (C) STEM image of $Li_xV_2O_5$ NR with a dashed box indicating a crack in the structure. (D) Corresponding EELS spectrum image (same scale as Figure 2C) spatially mapping the signal from the Li K edge resonance. The brighter spots correspond to the higher Li signal, notably around the edges of the NR and the crack inside the dashed box.

capacity of the NRs.[21] Lithium intercalates along the $a-b$ plane into the interlayer space following the equation: $V_2O_5 + xLi^+ + xe^- \rightarrow Li_xV_2O_5$.

To characterize the chemical composition change, we performed EELS studies using a 200 kV dedicated scanning transmission electron microscope (STEM) Hitachi HD-2300 installed with a Gatan Enfina spectrometer (Supporting Information). The EELS spectra taken on single V_2O_5 NRs before (pristine) and after 2 h lithiation ($Li_xV_2O_5$) are shown in Figure 2A and B, respectively. Here signal strength is plotted against electron energy loss. The background (pink) is extrapolated using the log-polynomial law fitting to produce the net signal of the NRs (green) from the overall signal (blue). The V M45-edge onset at ∼37 eV was observed in both pristine and lithiated phases, but a resonance

attributed to the Li K-line at ~62 eV was observed only in the $Li_xV_2O_5$ NRs, indicating the presence of Li in the NRs.

To obtain information on Li distribution in NRs after insertion, we performed EELS spatial mapping on single NRs with <10 nm resolution. Figure 2C shows a STEM image of a single $Li_xV_2O_5$ NR with $H = \sim 150$ nm. From the STEM−EELS data, the signal from the Li K edge can be extracted and mapped. The Li signal is shown in Figure 2D, with brighter areas corresponding to higher Li signal.

The EELS mapping of the lithiated V_2O_5 NR showed that the lithium was distributed across the entire NR, although there were notable regions of higher Li concentration found along the edges of the NR. This is because the edge of the NR had direct contact with BuLi and Li diffused into the NR from the edge. We note that there appeared to be a defect in the center, corresponding to a crack in the NR (Figure 2C, dashed box). Importantly, the Li concentration at the location close to the crack was also significantly higher than other parts of the NR (Figure 2D, dashed box), suggesting that the crack also had direct contact with BuLi. These results are consistent with the decreased Li insertion distance at the nanoscale size due to the large interfacial contact area. The nonuniform Li distribution does not change with time (after several days), indicating that an activation energy barrier exists for Li diffusion.

In bulk materials, lithium insertion into V_2O_5 can induce drastic changes in the crystal structure (Figure 3A). Several room-temperature phases[22] of $Li_xV_2O_5$ have been observed depending on the lithium content: the α- and ϵ-phases are observed for $x < 0.1$ and $0.35 < x < 0.7$, accompanied by an orthorhombic phase with increased puckering in the layers. The δ-phase at $x = 1$ results from one layer gliding out of two. At $x > 1$, the irreversible γ-phase is formed.

Increasing x to 3 causes the formation of the rock-salt ω-phase. In the bulk, $Li_3V_2O_5$ can be reversibly cycled as the ω-phase, but a large fraction of the lithium cannot be removed, causing a decrease in energy capacity. To observe these structural transformations, we performed TEM studies on individual NRs. Conventional bulk techniques such as XRD and electrochemical characterization give averaged structural information and often are insensitive to localized phase transformations.[23] On a V_2O_5 NR with $H = 100$ nm (Supporting Information) and $W = 230$ nm after 2 h Li treatment, TEM images show large contrast differences distributed over the entire nanoribbon (Figure 3B). Compared with the uniform contrast in pristine V_2O_5 NRs, large contrast differences suggest that spatial inhomogeneities exist. High-resolution TEM images show fringes with spacings in the range of 0.9−2.5 nm, significantly larger than any V_2O_5 lattice plane spacings. Instead, these fringes correspond to Moiré patterns,[24] which result from the interference of two superimposed structures with same lattice spacings but slight misorientation, or the same orientation but slight differences in lattice spacing. SAED revealed a diffraction pattern with 4-fold symmetry (Figure 3C, inset) with lattice spacing of 2.02 Å, matching that for the (200) plane of cubic ω-$Li_3V_2O_5$.[28] Inductively coupled plasma (ICP) atomic absorption spectroscopy measurements on the lithiated NRs agreed with this stoichiometry (Supporting Information). We also note that the spots in the diffraction patterns are elongated, consistent with the formation of Moiré patterns. The Moiré patterns strongly suggest the presence of misorientation domains along the *c*-axis or layer-stacking direction. In addition, the spot diffraction pattern rotated as the electron beam moved along the length of the ribbon, suggesting that the NRs are single crystalline-like but have disorder in the *a*−*b* planes as well. We believe that inhomogenous structural transformation upon Li intercalation, which has been confirmed with Raman spectroscopy[25,26] and electromagnetic pulse resonance,[27] causes large strain in the *a*-, *b*-, and *c*-axes and subsequent disordered phase domains.

To observe how the NR widths affect the structural transformation, we performed TEM studies on different widths of doped V_2O_5 NRs having the same thickness. Some V_2O_5 NRs showed a variation of width along the length of the same NR, making them ideal candidates for this purpose. Figure 3D shows a TEM image of a 2 h BuLi treated NR with $H = \sim 150$ nm and W ranging from 400 nm at location 1, 2.5 μm at location 2, to 3.5 μm at location 3. Significantly, SAED shows there is a dramatic variation of phases at the different locations. At location 1 (Figure 3E), the SAED spots due to ω-$Li_3V_2O_5$ (red circles) dominate the diffraction pattern, but another intermediate phase, γ-$Li_2V_2O_5$ (blue), is also identified. At location 2 (Figure 3F), both ω- and γ-$Li_3V_2O_5$ coexist. Compared to location 1, however, the SAED spots are elongated to the extent that some ring patterns form, suggesting a more disordered structure of the coexisting phases. At location 3 (Figure 3G), the diffraction intensity of pristine orthorhombic V_2O_5 (yellow) and ω-$Li_3V_2O_5$ is similar, suggesting that both phases exist in similar amounts. These results agree with previous studies done on micron-sized V_2O_5 particles,[28] where for larger particles, the homogenization of lithium throughout the lattice is slower, with lithium accumulating at the surface first and then additional Li diffusing into the interior. Our EELS data show lithium-rich areas at the edges of the NRs, and the SAED supports the presence of mixed phases with different Li content. For the narrower regions 1 and 2, the short Li diffusion lengths allowed more Li to diffuse into the interior after the Li-rich ω-$Li_3V_2O_5$ phase formed. In region 3, however, the presence of the pristine phase only (no lower Li phases) even after several days had passed indicates that additional Li could not diffuse past the ω-$Li_3V_2O_5$ into the interior, suggesting existence of a diffusion barrier. We attribute this diffusion barrier to the strain caused by the interface of the ω-$Li_3V_2O_5$ and V_2O_5 phases, which was more easily overcome in the narrower regions than the wider region 3. It should be noted that, although the same phases were observed in regions 1 and 2, the lattice was more disordered in region 2, suggesting that maintaining crystallinity in the phase transformation is more facile in the nanometer rather than micron dimension.

The effect of H (the *c*-axis dimension) on the Li insertion process is often overlooked and has not been previously studied. The above results were observed in NRs with large H (100−150 nm). Here we evaluate this dependence in our

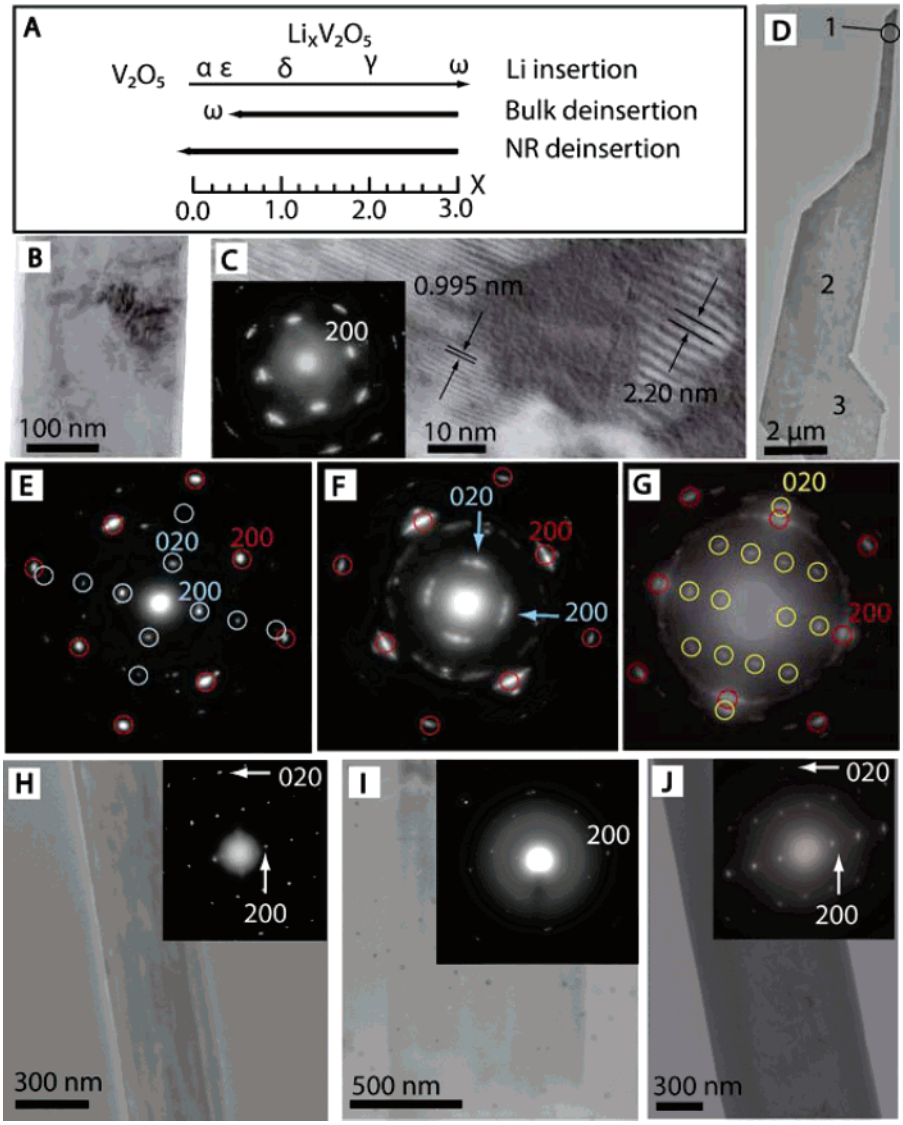

Figure 3. (A) Schematic of different $Li_xV_2O_5$ phases corresponding to the amount of Li inserted (x) per V_2O_5 unit. During Li intercalation, V_2O_5 adopts the α- through ω-$Li_xV_2O_5$ phases. During delithiation in the bulk, the structure remains in the ω-phase and Li is removed to $x = 0.4$. However, in our NRs, the ω-phase is transformed back to the original pristine V_2O_5 with a full removal of Li. (B) Low-magnification TEM image of a 100 nm thick $Li_xV_2O_5$ NR showing contrast differences indicating structural inhomogeneity. (C) High-resolution TEM image of $Li_xV_2O_5$ NR with cubic SAED taken along the ⟨001⟩ zone axis. The contrast differences and Moiré patterns with spacings of 0.995 and 2.20 nm are present. (D) 150 nm thick $Li_xV_2O_5$ NR with different SAED patterns at different widths along its ⟨020⟩ direction. Location 1 corresponds to a width of 400 nm, location 2 is 2.5 μm, and location 3 is 3.5 μm. (E−G) SAED of the locations 1−3 showing different phases at different NR widths. The zone axis is the ⟨001⟩. The ω-$Li_3V_2O_5$ cubic structure is present in all locations and is indicated by the red circles. (E) SAED at location 1. The blue circles match the γ-$Li_2V_2O_5$ orthorhombic structure. (F) SAED at location 2. The fainter, elongated spots marked with blue arrows as well as the broad ring correspond to γ-$Li_2V_2O_5$. (G) SAED at location 3. The yellow spots correspond to pristine V_2O_5, indicating that this region has unlithiated domains coexisting with ω-$Li_3V_2O_5$. (H) 100 nm thick and 400 nm wide NR treated with BuLi for 10 s and the SAED along the ⟨001⟩ zone axis in the inset. The (020) and (200) spots present match those for pristine V_2O_5, indicating that Li insertion did not take place. (I) 20 nm thick and 740 nm wide V_2O_5 NR treated with BuLi for 10 s and SAED (inset) with ω-$Li_3V_2O_5$ as the dominant phase. The (200) spot of ω-$Li_3V_2O_5$ is shown in SAED. (J) Low-magnification TEM image of $Li_xV_2O_5$ nanoribbon after treatment with Br_2. Inset: SAED is the orthorhombic structure for pristine V_2O_5, indicating a full delithiation and complete reversibility.

V_2O_5 NRs by BuLi treatment to study the rate of intercalation.[21] NRs of different thicknesses were treated with BuLi for a much shorter time, only 10 s (Supporting Information). For $H = 100$ nm thick and $W = 400$ nm wide NR, only the pristine V_2O_5 phase was observed (Figure 3H), suggesting that no significant amount of Li diffused into the NR layers. However, for a wider NR ($W = 740$ nm) with much smaller height ($H = \sim 20$ nm), ω-$Li_3V_2O_5$ was clearly observed as the dominant phase (Figure 3I). The data indicate that the thickness in the c-axis has a significant impact on the Li insertion process. Using the Li-ion diffusion coefficient reported for bulk V_2O_5 ($D_{Li} = 10^{-12}$ cm^2/s),[29] we estimate that the time required for Li to diffuse completely into a 740 nm wide NR is 1.5 h, which is ∼3 orders of magnitude longer than what we observed in thin NRs. We think that the ability of simultaneous structural transformation is

important in the Li insertion process. The transformation requires a crystal lattice distortion in all three dimensions to accommodate the ions, which can cause significant strain energy.[22] In thinner NRs, the activation barrier for this distortion is decreased relative to the bulk, making it easier to relax the strain, promoting faster transformation and thus faster Li-ion diffusion. These phenomena have not been observed before and are significant for fabricating batteries with much higher power density and longer cycle life.

Delithiation, the reverse process to Li insertion, is also important for complete rechargeable battery cycles. Delithiation in ω-$Li_xV_2O_5$ was achieved by treating NRs with Br_2 (Supporting Information), and the characterization was carried out with TEM. The delithiation occurs by the following equation: $Li_xV_2O_5 + 0.5xBr_2 \rightarrow V_2O_5 + x$LiBr. SAED revealed that the NRs can be delithiated back to the original, pristine, single-crystalline, orthorhombic phase of V_2O_5 (Figure 3J). This suggests that delithiation in our ω-$Li_xV_2O_5$ NRs is completely reversible. This is another new exciting observation and is a great advantage over the bulk ω-$Li_3V_2O_5$, where electrochemical delithiation is still limited to the ω-phase, with the lithium content remaining at $x = 0.4$ (Figure 3A).[29] In the bulk, using Br_2 can remove the lithium to $x = 0.1$, but the resulting material has adopted a disordered cubic structure.[22] Our results suggest that lithium intercalated in V_2O_5 NRs can be fully removed to the original charged state while maintaining the structural integrity of a single crystal. On the basis of the V_2O_5 discharge curve,[22] this full reversibility implies an increased capacity of 17% and expands the high-end voltage range because the $Li_xV_2O_5$ charge at $x = 0$ is 4 V. The energy density is estimated to be greatly increased by ~30%.

High-performance batteries require not only fast Li insertion/deinsertion but also efficient electronic conduction to facilitate efficient charging. Therefore, we carried out electron transport measurements on individual NRs before and after lithiation to correlate electronic behavior with structural changes. Individual pristine V_2O_5 NRs were contacted with four metal electrodes (10 nm Cr and 150 nm Au) defined by electron-beam lithography (Figure 4A) (Supporting Information). The current (I) versus voltage (V) characteristics were linear and symmetric, with a two-probe resistance of 9.5 MΩ (Figure 4b, dashed line). To extract the intrinsic NR resistance from the contact resistance, we also carried out four-probe measurements (Figure 4B, solid line). The intrinsic NR resistance is 9.04 MΩ, and the contact resistance is 0.46 MΩ. An intrinsic conductivity of 0.8−3.4 S/cm was obtained for ~20 NR devices tested. This conductivity is much higher than the bulk single crystalline value of 0.02 S/cm[30] and indicates an improved carrier transport pathway in the NR, possibly due to high crystallinity of the NR. After Li intercalation, the two-probe and four-probe *IV* characteristics were measured on the same NRs (Figure 4C). The intrinsic resistance is 6.3 GΩ with a contact resistance of 3.4 GΩ. The intrinsic conductivity of the individual $Li_xV_2O_5$ NRs is ~0.001 S/cm, 3 orders of magnitude lower than for pristine V_2O_5 NRs. This lowered conductivity and increased contact resistance may have been

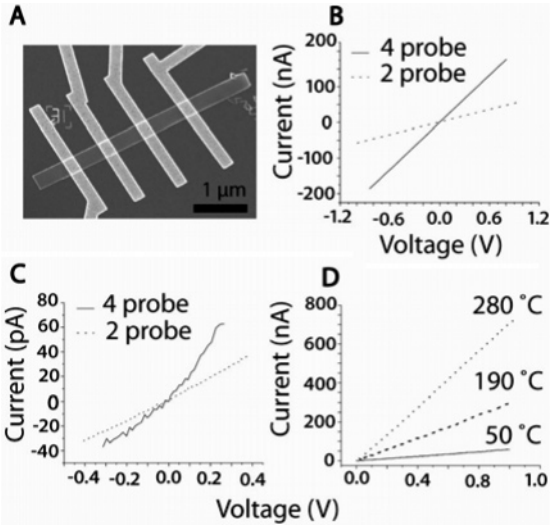

Figure 4. (A) SEM image of single NR contacted by four metal electrodes. (B−D) Current/voltage characteristics of individual NRs. (B−C) are measurements performed on the same NR. (B) Two- and four-probe *IV* characteristics for pristine V_2O_5 NR. (C) Two and four-probe *IV* characteristics for $Li_xV_2O_5$ NR treated with BuLi for 2h. (D) *IV* characteristics for pristine V_2O_5 NR at different temperatures, showing that the NR is stable at high temperatures.

due to mixed phases acting as barriers to efficient electron conduction or changes in local electronic structure, which will be further investigated. However, even given this lower conductivity, the *IV* characteristics remained linear and stable cycling between −6 to +6 V. If considering electronic transport only, we estimate that it would take less than 4.5 s to charge a single NR at 4 V, which is well suited for high-power battery applications. To evaluate whether efficient conduction can be maintained at higher temperature conditions, which can exist with joule heating in battery operation, we have carried out temperature-dependent measurements on individual V_2O_5 NRs (Figure 4D). The *IV* curves remain linear from room temperature to 280 °C. The conductance increases with increasing temperature, consistent with the semiconducting behavior of V_2O_5. The NR devices were stable at 280 °C, suggesting that V_2O_5 NR electrodes will be stable even under battery heating.

Our single V_2O_5 NR studies show exciting, ultrafast Li diffusion, completely reversible Li intercalation/deintercalation, and efficient electron transport. These results provide important, new information for a better Li battery design. For example, a NR battery architecture consisting of vertical arrays of NRs with small heights in which every NW has direct electrical contact with a collector electrode, can provide a super high power rate (360 C, or 10 s) because the power rate of the whole battery is limited by charging/discharging single NRs. In addition, the NR battery can have a larger energy density, longer life cycles, and better operation safety.

Acknowledgment. We thank A. Marshall, M. O'Connell, and G. Li for helpful discussion. Y. Cui acknowledges support from the Stanford New Faculty Startup Fund and the CPN seed fund. C. Chan acknowledges support from a National Science Foundation Graduate Fellowship and Stanford Graduate Fellowship.

Supporting Information Available: Experimental methods and materials, X-ray diffraction and atomic force microscope images of V_2O_5 nanoribbons. This material is available free of charge via the Internet at http://pubs.acs.org.

References

(1) Kang, K.; Meng, Y. S.; Berger, J.; Grey, C. P.; Ceder, G. *Science* **2006**, *311*, 977−980.
(2) Chung, S.-Y.; Bloking, J. T.; Chiang, Y.-M. *Nat. Mater.* **2002**, *1*, 123−128.
(3) Aricò, A. S.; Bruce, P.; Scrosati, B.; Tarascon, J.-M.; Van Schalkwijk, T. *Nat. Mater.* **2005**, *4*, 366−377.
(4) Patrissi, C. J.; Martin, C. R. *J. Electrochem. Soc.* **1999**, *146*, 3176−3180.
(5) Takahashi, K.; Limmer, S. J.; Wang, Y.; Cao, G. *J. Phys. Chem. B* **2004**, *108*, 9795−9800.
(6) Spahr, M. E.; Stoschitzki-Bitterli, P.; Nesper, R.; Haas, O.; Novák, P. *J. Electrochem. Soc.* **1999**, *146*, 2780−2783.
(7) Taberna, P. L.; Mitra, S.; Poizot, P.; Simon, P.; Tarascon, J.-M. *Nat. Mater.* **2006**, *5*, 567−573.
(8) Nam, K. T.; Kim, D.-W.; Yoo, P. J.; Chiang, C.-Y.; Meethong, N.; Hammond, P. T.; Chiang, Y.-M.; Belcher, A. M. *Science* **2006**, *312*, 885−888.
(9) Armstrong, G.; Armstrong, A. R.; Bruce, P. G.; Reale, P.; Scrosati, B. *Adv. Mater.* **2006**, *18*, 2597−2600.
(10) Rolison, D. R.; Dunn, B. *J. Mater. Chem.* **2001**, *11*, 963−980.
(11) Poizot, P.; Laruelle, S.; Grugeon, S.; Dupont, L.; Tarascon, J.-M. *Nature* **2000**, *407*, 496−499.
(12) Cui, Y.; Zhong, Z.; Wang, D.; Wang, W. U.; Lieber, C. M. *Nano Lett.* **2003**, *3*, 149−152.
(13) Law, M.; Greene, L. E.; Johnson, J. C.; Saykally, R.; Yang, P. *Nat. Mater.* **2005**, *4*, 455−459.
(14) Thelander, C.; Mårtensson, T.; Björk, M. T.; Ohlsson, B. J.; Larsson, M. W.; Wallenberg, L. R.; Samuelson, L. *Appl. Phys. Lett.* **2003**, *83*, 2052−2054.
(15) Murphy, D. W.; Christian, P. A.; DiSalvo, F. J.; Waszczak, J. V. *Inorg. Chem.* **1979**, *18*, 2800−2803.
(16) Whittingham, M. S. *J. Electrochem. Soc.* **1976**, *123*, 315−320.
(17) Li, W.; Garofalini, S. H. *J. Electrochem. Soc.* **2005**, *152*, A364−A369.
(18) Livage, J. *Coord. Chem. Rev.* **1998**, *178*−*180*, 999−1018.
(19) Le, D. B.; Passerini, S.; Guo, J.; Ressler, J.; Owens, B. B.; Smyrl, W. H. *J. Electrochem. Soc.* **1996**, *143*, 2099−2104.
(20) Ostermann, R.; Li, D.; Yin, Y.; McCann, J. T.; Xia, Y. *Nano Lett.* **2006**, *6*, 1297−1302.
(21) Whittingham, M. S.; Dines, M. B. *J. Electrochem. Soc.* **1977**, *124*, 1387−1388.
(22) Delmas, C.; Cognac-Auradou, H.; Cocciantelli, J. M.; Ménétrier, M.; Doumerc, J. P. *Solid State Ionics* **1994**, *69*, 257−264.
(23) Shao-Horn, Y. In *Lithium Batteries: Science and Technology*; Nazri, G.-A., Pistoia, G., Eds.; Kluwer Academic/Plenum: Boston, 2004; Chapter 16, pp 479−480.
(24) Williams, D. B.; Carter C. B. *Transmission Electron Microscopy*; Plenum: New York, 1996.
(25) Ramana, C. V.; Smith, R. J.; Hussain, O. M.; Massot, M.; Julien, C. M. *Surf. Interface Anal.* **2005**, *37*, 406−411.
(26) Baddour-Hadjean, R.; Raeklekboom, E.; Pereira-Ramos, J.-P. *Chem. Mater.* **2006**, *18*, 3548−3556.
(27) Pecquenard, B.; Gourier, D.; Baffier, N. *Solid State Ionics* **1995**, *78*, 287−303.
(28) Cocciantelli, J. M.; Ménétrier, M.; Delmas, C.; Doumerc, J. P.; Pouchard, M.; Broussely, M.; Labat, J. *Solid State Ionics* **1995**, *78*, 143−150.
(29) Leger, C.; Bach, S.; Soudan, P.; Pereira-Ramos, J.-P. *J. Electrochem. Soc.* **2005**, *152*, A236−A241.
(30) Allersma, T.; Hakim, R.; Kennedy, T. N.; MacKenzie, J. D. *J. Chem. Phys.* **1967**, *46*, 154−160.

NL062883J